Fused filament fabrication 3D printing of reactive porous media

Ishan S. Anjikar[1], Shelby Wales[2], Lauren E. Beckingham[1]

[1]Department of Civil Engineering, Auburn University, Auburn, AL 36849

[2]Department of Chemical Engineering, Auburn University, Auburn, AL, 36849

Corresponding author: Lauren Beckingham (leb@auburn.edu)

Key Points:

- 3D printing was used to create reactive rock samples.
- Custom reactive filament was made using calcite and HIPS mixtures.
- Accessible calcite surface area in 3D printed samples are comparable to real rock samples.

Abstract

Understanding the impacts of porous media properties on geochemical reactions is challenging due to the highly heterogeneous nature of natural samples. This work explores the use of 3D printing to create synthetic rock samples with reactive properties mimicking those of natural samples. Here, X-ray Computed Tomography and 3D printing were used to recreate the pore network structure and reactive properties of a Paluxy sandstone. Novel, reactive filaments for 3D printing synthetic rock samples were constructed from mixtures of high impact polystyrene and calcite. The distribution and accessible calcite surface area of printed samples were evaluated and compared to values for the real rock sample. Only a small fraction of the total calcite was on the surface of the printed sample but the accessible calcite surface area was comparable to real samples such that 3D printing may be a feasible means of fabricating reactive porous media samples.

Plain Language Summary

Geochemical reactions are important part of sub-surface systems. Understanding reactions rates and impacts in natural systems, however, is challenging given the highly heterogenous nature of natural samples. Laboratory experiments are often used to examine the impact of variations in conditions but are extremely challenging due to variations in natural porous media samples. To resolve this issue, 3D printing is explored here as a means of creating porous media samples with properties similar to actual samples. Rock samples were 3D printed based on images of a real rock sample using custom reactive filament made from mixtures of calcite grains and polymer pellets. The properties of the 3D printed samples were compared with the natural sample. The results showed that 3D printing can be used to create rock samples with comparable reactive surface areas, thus providing enhanced experimental capabilities to increase understanding of geochemical reactions in porous media.

1 Introduction

Contaminant transport (Essaid et al., 2015; Goh & Lim, 2004; Sandhu et al., 2018), microbiological reactions (Hunter et al., 1998; Jin & Bethke, 2005), acid injection for enhanced oil recovery (Zhu et al., 2018) and CO_2 injection into deep saline aquifers (Bachu et al., 1994; Beckingham et al., 2017; Black et al., 2015; Deng et al., 2015; De Silva et al., 2015; Xiong et al., 2018) can result in geochemical reactions in subsurface systems. These reactions can have a

significant impact on the chemical and physical properties of the system, altering formation fluid chemistry and porosity and permeability (Beckingham et al., 2013; Rathnaweera et al., 2016; Ross et al., 1982; Shiraki & Dunn, 2000; Yu et al., 2012). Even though there is good understanding of the changes in porosity due to dissolution/precipitation reactions (Deng et al., 2015; Zou et al., 2018), there are large imprecisions in estimation of mineral reaction rates in porous media systems (Bachu et al., 2007; Beckingham et al., 2016; Bourg et al., 2015; Jung & Navarre-Sitchler, 2018; Wen & Li, 2018), Mineral dissolution rates have been typically estimated from laboratory experiments that use disaggregated pure mineral phases (Liteanu & Spiers, 2009; Zhang et al., 2002) that are fundamentally unable to reflect the reaction conditions in real porous media samples. Reaction rates in porous media have been observed to depend on the pore structure (Pereira Nunes et al., 2016), accessible mineral surface area (Beckingham et al., 2017), flow paths and concentration gradients (Molins et al., 2012). 2D microfluidic devices have also emerged as a promising way of enhancing understanding of reaction rates in porous media (Soulaine et al., 2018; Yoon et al., 2019) but are often based on simplified geometries. Some laboratory experiments have estimating rates using physical core or rock samples. However, replicate experiments aimed at discerning the impacts of individual parameters on rates is challenging as these experiments often lead to the sample being disturbed or destroyed, thus ceasing its use for another experiment (Ameloot et al., 2016; Bultreys et al., 2016; Elhami et al., 2016; Josh et al., 2012; Vishal et al., 2015). Another sample from the same formation can be used, which has similar chemical properties, but no two samples have identical pore structures (Al-Khulaifi et al., 2018; Liu et al., 2017).

Additive manufacturing (AM) or 3D printing has emerged as a powerful tool to create porous media samples with controlled features and even identical pore structures (Ishutov et al., 2018; Kong et al., 2019). AM is the process of joining materials to make parts from 3D model data (International, 2015), usually layer upon layer as in Fused Deposition Modeling (FDM)/fused filament fabrication (FFF) (Guo & Leu, 2013). 3D printing has been widely used in aerospace, automotive, biomedical, and art fields (Ligon et al., 2017), and has been recently used for fabricating microfluidic devices (Bhattacharjee et al., 2016; Mcdonald & Whitesides, 2002; Rusling, 2018; Watson et al., 2018) and bench scale flow through reactors for water treatment (Loeb et al., 2019). The potential use of 3D printing for fabricating geological materials for use in lab experiments has been considered for undisturbed soil samples (Bacher et al., 2015; Dal Ferro

& Morari, 2015; Otten et al., 2012), and sedimentary rocks (Ishutov et al., 2015; Kong et al., 2019), where the research was focused on replicating the pore network of natural samples. The applicability of 3D printed samples to replicate flow properties, namely bulk porosity and permeability (Head & Vanorio, 2016) and rock mechanics (Hodder et al., 2018; C. Jiang & Zhao, 2015; L. Jiang et al., 2020; Q. Jiang et al., 2016) has also been investigated. Although the use of 3D printing is growing in geoscience applications, the feasibility of 3D printing to be utilized in geochemically reactive systems has never been considered.

This work explores the utility of FFF technology for 3D printing synthetic porous media samples with porosity and calcite accessible surface area mimicking natural samples to enhance understanding of geochemical reactions in porous media. Using this approach, samples with identical pore structures could be created and used in experiments devised to isolate the role of individual parameters on mineral reactions and reaction rates in porous media, eliminating experimental uncertainties that exist even with two samples from the same location. Here, novel calcite-containing filament with varying weight percentages of calcite are created. Synthetic rock samples are then printed using these custom filaments based on the pore structure of a sandstone sample. The distribution and accessible surface area of calcite in the 3D printed samples is then computed from 2D and 3D images of the printed samples.

2 Materials and Methods

2.1 Filament Preparation

High Impact Polystyrene (HIPS) and Acrylonitrile Butadiene Styrene (ABS) were considered as the basis for filament construction. To ensure the stability of the printed samples in acidic reaction conditions, such as those pertinent for acid mine drainage, geologic CO_2 sequestration, etc., the stability of these materials in acid solution was first examined. Batch experiments where 3D printed HIPS and ABS cubes were kept in an HCl solution of pH 3.5 for up to 7 days were carried out where further details on acid resistance testing are in the SI. While both cubes were relatively unreactive in acid, smaller changes in pH and weight were observed for HIPS such that it was selected as the filament base material.

Reactive filaments were made by mixing known weights of powdered Iceland spar calcite and HIPS 8 MELT 2 IZOD pellets (3DXTech). Iceland spar calcite has been used in many calcite dissolution experiments (Molins et al., 2014; Peng et al., 2015; Plummer & Wigley, 1976) because of its purity. Here, calcite crystals were crushed, powdered and segregated into 63-90 μm size particles using ASTM sieves no. 170 and 230. HIPS pellets and segregated calcite powder were mixed together to obtain batches with calcite weight fractions of 5%, 10%, 15% and 20%. The volume fraction of calcite in each batch was also calculated using bulk densities of HIPS and Iceland spar calcite (Table S1). The bulk density of HIPS used is 1.04 g/cm^3 and that of Iceland spar calcite is 2.71g/cm^3 (Lambkin et al., 2011). Each HIPS/calcite batch was loaded into the hopper of Filabot EX2 filament extruder and extruded into filament at a temperature of 210°C. The filament extrusion rate was controlled to achieve a filament thickness of approximately 2.6 mm.

2.2 Mesh generation from 3D X-ray CT image

A sandstone sample from the Paluxy formation in Kemper county, Mississippi considered in Qin and Beckingham (2019) was selected here as the basis for 3D printing. This sample was extracted from well MPC 34-1 from a depth of 1541 m. 3D X-ray CT images collected on a 0.5 cm x 0.5 cm x 1 cm cuboid at a resolution of 6.62 microns and segmented in Qin and Beckingham (2019) were utilized here. The original X-ray CT image stack, with porosity of 0.26, was subsampled here to extract a 100 x 100 x 100 voxel cube. A wavefront (.obj) mesh, which creates a mesh using marching cubes, for the grains was then generated with ImageJ, an open source image processing software. The mesh was then processed in Blender, an open source 3D creation software, to remove unconnected grains. The resulting mesh was then enlarged by twenty times to ensure that all the pores could be reproduced properly when printing and then exported as a stereolithography (.stl) file.

2.3 3D printing of rock samples

To prepare for 3D printing, the mesh files were first converted into a 3D printer supported format, gcode, using Cura v3.2.27. Before deciding on the final print settings, various printing conditions were tested. Samples were printed using a Lulbotz Taz4 printer with bed temperature set at 100°C, 110°C and 120°C, nozzle temperature at 230°C and 240°C, layer thickness and height

of 0.2 mm, 0.25 mm and 0.3 mm and 40%, 50%, 60% and 100% fan speed with an objective of printing samples with low internal porosity and avoiding nozzle clogging.

Based on visual inspection of the test samples printed with different printing conditions, the final printing conditions were selected: nozzle temperature of 240°C, bed temperature of 110°C from 0.5 mm nozzle with 100% infill, 50% fan speed, and a layer thickness and height of 0.25 mm. Three reactive sample sets were then printed using three different custom filaments, those containing 5%, 10% and 15% calcite. Identical printing conditions were used for printing with each filament. Each sample set consisted of two replicate cubes where one cube was used for subsequent Scanning Electron Microscopy (SEM) analysis and the other was used for X-ray CT analysis.

2.4 Image analysis of 3D printed samples

2.4.1 2D imaging analysis

3D printed samples were imaged using 2D scanning electron microscopy (SEM) operated in backscatter electron (BSE) mode using a ZEISS EVO 50VP Scanning Electron Microscope at Auburn University to examine the distribution of calcite on the printed sample. Before imaging, samples were coated with carbon using an EMS 550X Sputter Coating Device. Images were collected at a resolution of 3 microns using a beam intensity of 20 kV.

2.4.2 3D imaging analysis

3D X-ray CT images were collected for the 5% and 15% calcite containing samples at a voxel resolution of 11 microns. Collected images were cropped to obtain a 900 x 900 x 900 voxel cube and segmented into pores, HIPS and calcite voxels. The voxels were segmented into grains and pores first and then the grains were segmented into calcite and HIPS. For each segmentation, the threshold was first calculated using the threshold optimization method in Peters (2009). The resulting threshold was then manually validated via ImageJ and modified as necessary (+/- 5 of calculated threshold value). Finally, an error reduction algorithm that flips lone voxels (Peters, 2009) was applied to reduce the misclassified pixels. Calcite voxels were further differentiated between those present on the surface i.e. in contact with the pores and those present inside the sample. The total porosity was calculated by counting the number of pore voxels in the segmented

image and dividing by the total number of voxels in the cube. The connected porosity was then determined using a marching cube and burning algorithm modified from Landrot et al. (2012) and Beckingham et al. (2017). The accessible calcite surface area was determined using the approach developed in Landrot et al. (2012). This involves first identifying calcite and HIPS voxels in contact with pore voxels. A mesh, generated from the segmented 3D X-ray images after image processing in ImageJ and mesh processing in Blender, was then applied to the pore-bordering surface of calcite and HIPS voxels and the surface area of the mesh was calculated by adding the area of individual faces on the mesh. The calcite surface area was calculated by multiplying the mesh surface area by the proportion of pore-bordering voxels corresponding to calcite. The total mass of calcite present in the sample was calculated by multiplying the total volume of calcite voxels by the bulk density of Iceland spar calcite. The normalized accessible calcite surface area then was determined by dividing the calcite surface area by the mass of calcite present in sample.

3 Results and Discussion

3.1 Filament Preparation

Optical microscope images of four filaments with varying calcite contents prepared for 3D printing are shown in Figure 1. Filament extrusion was highly influenced by the amount of calcite mixed with HIPS. As the amount of calcite increased in the mixture, maintaining desired filament thickness and uniformity became difficult. In addition, an increase in filament stiffness was observed with increasing calcite content. Maintaining uniform composition of the filament was also challenging and calcite agglomeration was prevalent in the filament made with 20% calcite. The 20% filament also had bubbles on its surface, thus it was not of acceptable quality to be used for 3D printing as the calcite agglomeration would result in nozzle clogging and surface defects in the filament would result in defects in the printed sample. Deviations in desired thickness were much less apparent in filaments with 5%, 10% and 15% calcite and they also maintained flexibility. As such, the 5%, 10%, and 15% calcite filaments were selected for 3D printing. Some deviations from the desired thickness of 2.6 mm were apparent sporadically in the 15% calcite filament and a section of the 15% calcite filament that maintained the desired thickness was isolated from the problematic areas and used for 3D printing.

Based on observed filament properties, the maximum amount of calcite that can be used with HIPS to create filament is between 15 - 20% by weight. As the amount of calcite increased in the filament, maintaining uniformity in the calcite distribution and filament thickness was increasingly challenging. Similar restrictions have been observed by Hodder et al. (2018) with respect to the amount of binder material that can be present in the sample.

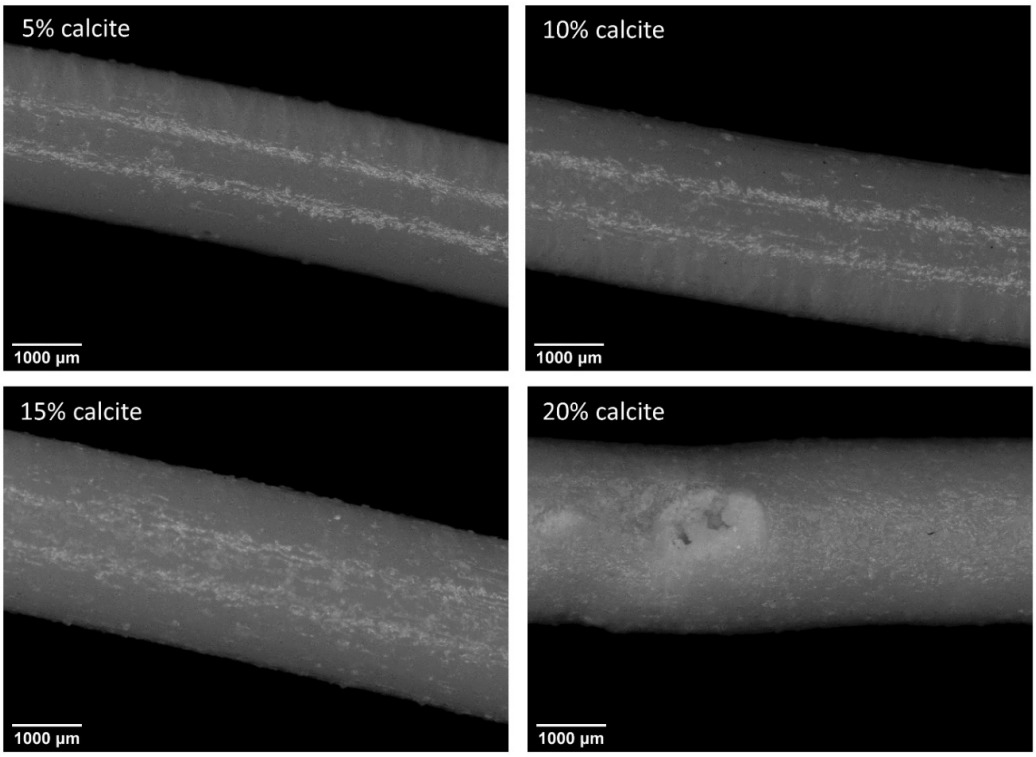

Figure 1. Optical microscope images of calcite-HIPS filaments with different weight fraction of calcite.

3.2 Mesh generation from 3D X-ray CT image

The thresholded 3D X-ray CT image of the Paluxy sandstone to be utilized as the basis for mesh generation is shown in Figure 2. The resulting mesh generated from the X-ray CT image after image and mesh processing is shown in Figure 2b. The mesh has a porosity of 0.2917 while the porosity of the X-ray CT sub-sample is 0.2652, which is similar to the experimentally measured porosity of 0.26 of the original sample. The higher porosity in the mesh resulted from removal of unconnected grains which cannot be printed with 3D printing.

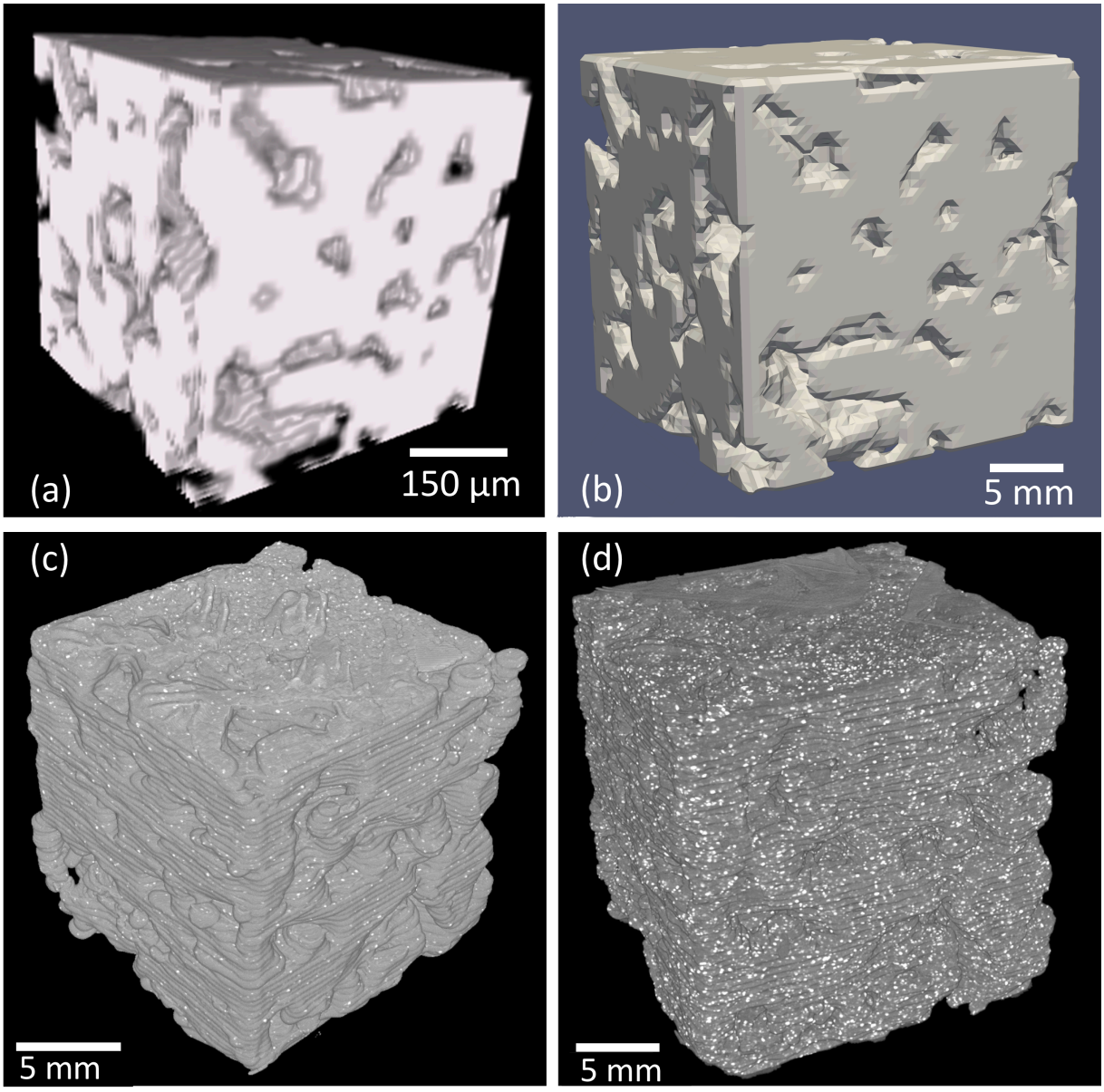

Figure 2 (a) Thresholded 3D X-ray CT image with grains in white, (b) 3D stereolithography mesh generated from X-ray CT images corresponding to grains and X-ray CT images of 3D printed samples made with filament containing (c) 5% calcite and (d) 15% calcite.

3.3 3D printing of rock samples

Figure S4 shows the 3D printed samples using the 5%, 10%, and 15% calcite filament. As evident in Figure S4, the printed layers in the 5% calcite sample have better overlap and transition and there are no gaps between printed layers. In the 10% (Fig. S4,b) and 15% (Fig. S4, c) calcite sample, there are periodic gaps in the printed layers and rows and these printing defects increased with calcite content.

3.4 Image analysis of 3D printed samples

3.4.1 SEM analysis

The SEM BSE images of the 5%, 10% and 15% calcite containing samples are shown in Figure S8. It should be noted that the images are not from the same section of the three cubes. The darker areas in these images correspond to pores and the brightest pixels corresponds to calcite. The remaining areas represent the HIPS. Calcite is easily distinguishable in these images (high intensity pixels) and is distributed on the surface of the printed structure and adjacent to pores. The fraction of calcite in to solid HIPs in the SEM images was similar for 10% and 15% sample (Fig. S8, Table S2). As such, only the 5% and 15% samples were selected for further 3D imaging analyses.

Also evident in these images are printing defects including incomplete overlap between layers and between rows in the same layer. These defects were more evident in the 15% sample as compared to 5% and 10% sample. Different printing temperatures were assessed as a means to reduce defects where the fewest defects were observed with the chosen printing temperature of 240°C (Figures S5-S7.).

3.4.2 X-ray CT analysis

X-ray CT images of the 5% and 15% calcite sample are shown in Figure 2. Brighter voxels correspond to calcite, grey to HIPS, and black to pores. As evident in the X-ray CT images, the amount of calcite is much higher in the 15% sample as compared to 5% sample. Table 1 shows the volume percentages of each component in 3D printed samples computed by counting voxels in the segmented X-ray CT images. The porosity of the 5% sample is 0.2812 and closer to that of the original sample (0.26) as compared to the 15% sample that has a porosity of 0.3371. The higher porosity in the 15% sample is due to an increase in unintended internal porosity due to printing

defects, which was also evident in the SEM images of the sample. It should also be noted that there may be micro porosity in the real sandstone sample and thus a similar resolution for the X-ray CT images of the sandstone and the 3D printed sample was used for better comparison. However, additional micro porosity was not evident via high-resolution SEM images. As such, this type of micro porosity it is not anticipated to be prevalent in the sample.

The amount of calcite in the printed samples agrees relatively well with the amount in the filament (Table 1). However, there is increase in the amount of calcite in the 5% sample as compared to what was used to make the filament. This is likely due to the non-uniform distribution of calcite in the filament where additional investigations are needed to determine how and if clumping can be prevented during filament fabrication.

Sample property	**5wt% calcite sample**	**15wt% calcite sample**	**Paluxy Sandstone Sample**
Calcite in filament (v%)	2.0	6.3	-
HIPS in printed solid (v%)	97.1	93.7	-
Calcite (in solid) (v%)	2.9	6.3	9.63
Inaccessible calcite (%)	99.60	99.83	22.74
Accessible calcite (%)	0.40	0.17	77.26
Total Porosity	0.2812	0.3371	0.2516
Connected Porosity	0.2812	0.3370	0.2338
Total accessible surface area	28.41×10^{-4} m^2	43.11×10^{-4} m^2	-
Accessible calcite surface area	8.03×10^{-6} m^2	6.80×10^{-6} m^2	-
Amount of calcite	5.55×10^{-2} g	11.06×10^{-2} g	-
Normalized accessible calcite surface area	1.45×10^{-4} m^2/g	0.62×10^{-4} m^2/g	8.13×10^{-4} m^2/g

Table 1. Sample properties calculated from the X-ray CT images of the 5% and 15% calcite 3D printed samples where accessible calcite refers to calcite adjacent to connected porosity.

The distribution of calcite between the printed surface and the internal printed volume in the 5% and 15% sample are also given in Table 1 where the calcite on the printed surface would be accessible for reactions. In both samples, the percentage of calcite present on the surface is less than 0.5%. The 5% calcite sample has 0.4% calcite on the surface while the 15% calcite sample

has 0.17% calcite on the surface. This may, however, reflect the accessibility of calcite in real samples where clay coatings may restrict surface accessibility (Landrot et al., 2012; Waldmann et al., 2014).

The total porosity, connected porosity, total accessible surface area, accessible calcite surface area and normalized accessible calcite surface area calculated from X-ray CT images of the 3D printed samples are given in Table 1. The connected porosity of the 5% sample and 15% samples are 0.2812 and 0.3370 respectively. There is not much decrease in connected porosity as compared to total porosity for both samples which indicates that the unintended internal pore space in the 15% sample is connected to the macro pore space. The total accessible surface area of the 5% and 15% samples are 28.41 x 10^{-4} m^2 and 43.11 x 10^{-4} m^2. The increase in total accessible surface area in the 15% calcite sample is due to the increased connected porosity in the sample. The accessible calcite surface area for the 5% and 15% samples is 8.03 x 10^{-6} m^2 and 6.80 x 10^{-6} m^2 respectively. Although the 15% sample has a higher porosity and almost 50% more total accessible surface area as compared to 5% sample, the accessible calcite surface area is higher in the 5% sample. This is due to the higher amount of calcite present on the surface in the 5% sample as compared to the 15% sample. The normalized accessible calcite area of the 5% and 15% sample are 1.45 x 10^{-4} m^2/g and 0.62 x 10^{-4} m^2/g respectively. In comparison with accessible calcite surface areas for real samples, the normalized accessible calcite surface area calculated here is within the values for natural samples but is an order of magnitude lower than those calculated for the Paluxy sandstone in Qin and Beckingham (2019) where the accessible calcite area was 8.13 x 10^{-4} m^2/g for a calcite volume fraction of 9%. The normalized accessible calcite surface areas for the 3D printed samples are higher as compared to values computed for a volcanogenic sandstone from the Haizume formation reported in Beckingham et al. (2017) where the sample contained 0.03% calcite by volume and the calcite accessible surface area was 2.14 x 10^{-5} m^2/g. Lower mineral accessible surface area in their sample was due to the presence of clay coatings on the mineral grains which reduced the accessibility of calcite.

4 Conclusions

This work explores the feasibility of 3D printing samples containing reactive minerals and properties reflecting those of natural samples. Rock structures with pore networks based on natural samples can be easily extracted from 3D X-ray CT images and serve as the basis for printed samples. Custom filaments containing mineral phases can be readily created in the laboratory using common materials with a maximum fraction of the reactive minerals of ~15%. Polymers suitable for 3D printing were tested for their compatibility to be used in acidic conditions typically found in environmental systems with geochemical reactions where neither polymer test exhibited significant signs of degradation. Created filaments can be utilized in FFF printing where these printers are low-cost and widely available. However, it should be noted that currently the distribution of reactive mineral within the printed structure can't be controlled and additional efforts are needed to increase uniformity of the mineral phase in the created filament. In addition, there can be problems associated with printing samples, such as generation of unintended internal porosity due to incomplete overlap between layers or within the same layer in the sample, particularly as the amount of mineral in the filament increases. In spite of these challenges, however, the properties of the printed porous media samples reflected those of real porous media. In particular, accessible calcite surface area was explored here as a reflection of the reactivity of the samples. The accessible calcite surface area of 3D printed samples agreed well with measured accessible calcite surface areas in other sandstone samples. As such, 3D printing may be a viable means of fabricating samples with representative accessible mineral surface areas. Further work, however, is needed to understand the surface properties of the printed samples in comparison to real samples.

This study made use of FFF technology for 3D printing. The possibility of achieving the same objective with other methods of 3D printing has yet to be explored and may offer some additional benefits and challenges to successful fabrication of synthetic reactive rocks. Further studies using FFF 3D printing are also needed to improve our understanding of the parameters affecting mineral distribution in the 3D printed rock samples and facilitate better control over mineral distribution.

Acknowledgments

Authors would like to acknowledge Dr. Eldon Triggs for allowing use of Lulbotz Taz4 3D printer and preliminary filament testing using their Filabot filament extruder. The author would also like to acknowledge undergraduate student Hayley Anderson for helping with the setup of acid resistance tests and filament fabrication. Sandstone samples and 3D imaging of sandstone was supported by U.S. Department of Energy's National Energy Technology Laboratory and cost-sharing partners under grant number FE0029465, "Establishing an Early CO2 Storage Complex in Kemper, Mississippi: Project ECO2S", managed by the Southern States Energy Board. Remaining 3D printing work supported by Auburn University. Data available on Open Science Framework DOI 10.17605/OSF.IO/XB6KY.

References

Al-Khulaifi, Y., Lin, Q., Blunt, M. J., & Bijeljic, B. (2018). Reservoir-condition pore-scale imaging of dolomite reaction with supercritical CO2acidified brine: Effect of pore-structure on reaction rate using velocity distribution analysis. *International Journal of Greenhouse Gas Control*, *68*(November 2017), 99–111. https://doi.org/10.1016/j.ijggc.2017.11.011

Ameloot, N., Maenhout, P., De Neve, S., & Sleutel, S. (2016). Biochar-induced N2O emission reductions after field incorporation in a loam soil. *Geoderma*, *267*, 10–16. https://doi.org/10.1016/J.GEODERMA.2015.12.016

Bacher, M., Schwen, A., & Koestel, J. (2015). Three-Dimensional Printing of Macropore Networks of an Undisturbed Soil Sample. *Vadose Zone Journal*, *14*(2), 0. https://doi.org/10.2136/vzj2014.08.0111

Bachu, S., Gunter, W. D., & Perkins, E. H. (1994). Aquifer disposal of CO2: Hydrodynamic and mineral trapping. *Energy Conversion and Management*, *35*(4), 269–279. https://doi.org/10.1016/0196-8904(94)90060-4

Bachu, S., Bonijoly, D., Bradshaw, J., Burruss, R., Holloway, S., Christensen, N. P., & Mathiassen, O. M. (2007). CO2 storage capacity estimation: Methodology and gaps. *International Journal of Greenhouse Gas Control*, *1*(4), 430–443. https://doi.org/10.1016/S1750-5836(07)00086-2

Beckingham, L., Steefel, C. I., Swift, A. M., Voltolini, M., Yang, L., Anovitz, L. M., et al. (2017). Evaluation of accessible mineral surface areas for improved prediction of mineral reaction rates in porous media. *Geochimica et Cosmochimica Acta*, *205*, 31–49. https://doi.org/10.1016/J.GCA.2017.02.006

Beckingham, L.E., Peters, C. A., Um, W., Jones, K. W., & Lindquist, W. B. (2013). 2D and 3D imaging resolution trade-offs in quantifying pore throats for prediction of permeability. *Advances in Water Resources*, *62*, 1–12. https://doi.org/10.1016/J.ADVWATRES.2013.08.010

Beckingham, Lauren E., Mitnick, E. H., Steefel, C. I., Zhang, S., Voltolini, M., Swift, A. M., et

al. (2016). Evaluation of mineral reactive surface area estimates for prediction of reactivity of a multi-mineral sediment. *Geochimica et Cosmochimica Acta*, *188*, 310–329. https://doi.org/10.1016/J.GCA.2016.05.040

Bhattacharjee, N., Urrios, A., Kang, S., & Folch, A. (2016). The upcoming 3D-printing revolution in microfluidics. *Lab on a Chip*, *16*(10), 1720–1742. https://doi.org/10.1039/c6lc00163g

Black, J. R., Carroll, S. A., & Haese, R. R. (2015). Rates of mineral dissolution under CO2storage conditions. *Chemical Geology*, *399*, 134–144. https://doi.org/10.1016/j.chemgeo.2014.09.020

Bourg, I. C., Beckingham, L. E., & DePaolo, D. J. (2015). The Nanoscale Basis of CO2 Trapping for Geologic Storage. *Environmental Science and Technology*, *49*(17), 10265–10284. https://doi.org/10.1021/acs.est.5b03003

Bultreys, T., De Boever, W., & Cnudde, V. (2016). Imaging and image-based fluid transport modeling at the pore scale in geological materials: A practical introduction to the current state-of-the-art. *Earth-Science Reviews*, *155*, 93–128. https://doi.org/10.1016/J.EARSCIREV.2016.02.001

Dal Ferro, N., & Morari, F. (2015). From Real Soils to 3D-Printed Soils: Reproduction of Complex Pore Network at the Real Size in a Silty-Loam Soil. *Soil Science Society of America Journal*, *79*(4), 1008. https://doi.org/10.2136/sssaj2015.03.0097

Deng, H., Fitts, J. P., Crandall, D., McIntyre, D., & Peters, C. A. (2015). Alterations of Fractures in Carbonate Rocks by CO2-Acidified Brines. *Environmental Science and Technology*, *49*(16), 10226–10234. https://doi.org/10.1021/acs.est.5b01980

Elhami, E., Ask, M., & Mattsson, H. (2016). Physical- and geomechanical properties of a drill core sample from 1.6 km depth at the Heletz site in Israel: Some implications for reservoir rock and CO2 storage. *International Journal of Greenhouse Gas Control*, *48*, 84–93. https://doi.org/10.1016/J.IJGGC.2016.01.006

Essaid, H. I., Bekins, B. A., & Cozzarelli, I. M. (2015). Organic contaminant transport and fate in the subsurface: Evolution of knowledge and understanding. *Water Resources Research*, *51*(7), 4861–4902. https://doi.org/10.1002/2015WR017121

Goh, K.-H., & Lim, T.-T. (2004). Geochemistry of inorganic arsenic and selenium in a tropical soil: effect of reaction time, pH, and competitive anions on arsenic and selenium adsorption. *Chemosphere*, *55*(6), 849–859. https://doi.org/10.1016/J.CHEMOSPHERE.2003.11.041

Guo, N., & Leu, M. C. (2013). Additive manufacturing: Technology, applications and research needs. *Frontiers of Mechanical Engineering*, *8*(3), 215–243. https://doi.org/10.1007/s11465-013-0248-8

Head, D., & Vanorio, T. (2016). Effects of changes in rock microstructures on permeability: 3-D printing investigation. *Geophysical Research Letters*, *43*(14), 7494–7502. https://doi.org/10.1002/2016GL069334

Hodder, K. J., Nychka, J. A., & Chalaturnyk, R. J. (2018). Process limitations of 3D printing model rock. *Progress in Additive Manufacturing*, *3*(3), 173–182. https://doi.org/10.1007/s40964-018-0042-6

Hunter, K. S., Wang, Y., & Van Cappellen, P. (1998). Kinetic modeling of microbially-driven redox chemistry of subsurface environments: coupling transport, microbial metabolism and geochemistry. *Journal of Hydrology*, *209*(1–4), 53–80. https://doi.org/10.1016/S0022-1694(98)00157-7

International, A. (2015). *ASTM ISO/ASTM52900-15 Standard Terminology for Additive Manufacturing – General Principles – Terminology*. West Conshohocken, PA. https://doi.org/10.1520/ISOASTM52900-15

Ishutov, S., Hasiuk, F. J., Harding, C., & Gray, J. N. (2015). 3D printing sandstone porosity models. *Interpretation*, *3*(3), SX49–SX61. https://doi.org/10.1190/INT-2014-0266.1

Ishutov, S., Hasiuk, F. J., Jobe, D., & Agar, S. (2018). Using Resin-Based 3D Printing to Build Geometrically Accurate Proxies of Porous Sedimentary Rocks. *Groundwater*, *56*(3), 482–490. https://doi.org/10.1111/gwat.12601

Jiang, C., & Zhao, G.-F. (2015). A Preliminary Study of 3D Printing on Rock Mechanics. *Rock Mechanics and Rock Engineering*, *48*(3), 1041–1050. https://doi.org/10.1007/s00603-014-0612-y

Jiang, L., Yoon, H., Bobet, A., & Pyrak-Nolte, L. J. (2020). Mineral Fabric as a Hidden Variable in Fracture Formation in Layered Media. *Scientific Reports*, *10*(1), 2260. https://doi.org/10.1038/s41598-020-58793-y

Jiang, Q., Feng, X., Song, L., Gong, Y., Zheng, H., & Cui, J. (2016). Modeling rock specimens through 3D printing: Tentative experiments and prospects. *Acta Mechanica Sinica*, *32*(1), 101–111. https://doi.org/10.1007/s10409-015-0524-4

Jin, Q., & Bethke, C. M. (2005). Predicting the rate of microbial respiration in geochemical environments. *Geochimica et Cosmochimica Acta*, *69*(5), 1133–1143. https://doi.org/10.1016/J.GCA.2004.08.010

Josh, M., Esteban, L., Delle Piane, C., Sarout, J., Dewhurst, D. N., & Clennell, M. B. (2012). Laboratory characterisation of shale properties. *Journal of Petroleum Science and Engineering*, *88–89*, 107–124. https://doi.org/10.1016/J.PETROL.2012.01.023

Jung, H., & Navarre-Sitchler, A. (2018). Scale effect on the time dependence of mineral dissolution rates in physically heterogeneous porous media. *Geochimica et Cosmochimica Acta*, *234*, 70–83. https://doi.org/10.1016/J.GCA.2018.05.009

Kong, L., Ostadhassan, M., Hou, X., Mann, M., & Li, C. (2019). Microstructure characteristics and fractal analysis of 3D-printed sandstone using micro-CT and SEM-EDS. *Journal of Petroleum Science and Engineering*, *175*, 1039–1048. https://doi.org/10.1016/J.PETROL.2019.01.050

Lambkin, D. C., Gwilliam, K. H., Layton, C., Canti, M. G., Piearce, T. G., & Hodson, M. E. (2011). Production and dissolution rates of earthworm-secreted calcium carbonate. *Pedobiologia*, *54*, S119–S129. https://doi.org/10.1016/J.PEDOBI.2011.09.003

Landrot, G., Ajo-Franklin, J. B., Yang, L., Cabrini, S., & Steefel, C. I. (2012). Measurement of accessible reactive surface area in a sandstone, with application to CO 2 mineralization. *Chemical Geology*, *318–319*, 113–125. https://doi.org/10.1016/j.chemgeo.2012.05.010

Ligon, S. C., Liska, R., Stampfl, J., Gurr, M., & Mülhaupt, R. (2017). Polymers for 3D Printing

and Customized Additive Manufacturing. *Chemical Reviews*, *117*(15), 10212–10290. https://doi.org/10.1021/acs.chemrev.7b00074

Liteanu, E., & Spiers, C. J. (2009). Influence of pore fluid salt content on compaction creep of calcite aggregates in the presence of supercritical CO2. *Chemical Geology*, *265*(1–2), 134–147. https://doi.org/10.1016/J.CHEMGEO.2008.12.010

Liu, K., Ostadhassan, M., Zhou, J., Gentzis, T., & Rezaee, R. (2017). Nanoscale pore structure characterization of the Bakken shale in the USA. *Fuel*, *209*(August), 567–578. https://doi.org/10.1016/j.fuel.2017.08.034

Loeb, S. K., Kim, J., Jiang, C., Early, L. S., Wei, H., Li, Q., & Kim, J.-H. (2019). Nanoparticle Enhanced Interfacial Solar Photothermal Water Disinfection Demonstrated in 3-D Printed Flow-Through Reactors. *Environmental Science & Technology*, acs.est.9b01142. https://doi.org/10.1021/acs.est.9b01142

Mcdonald, J. C., & Whitesides, G. M. (2002). Poly(dimethylsiloxane) as a Material for Fabricating Microfluidic Devices. *ACCOUNTS OF CHEMICAL RESEARCH*, *35*(7), 491–499. https://doi.org/10.1021/ar010110q

Molins, S., Trebotich, D., Steefel, C. I., & Shen, C. (2012). An investigation of the effect of pore scale flow on average geochemical reaction rates using direct numerical simulation. *Water Resources Research*, *48*(3), 1–11. https://doi.org/10.1029/2011WR011404

Molins, S., Trebotich, D., Yang, L., Ajo-Franklin, J. B., Ligocki, T. J., Shen, C., & Steefel, C. I. (2014). Pore-scale controls on calcite dissolution rates from flow-through laboratory and numerical experiments. *Environmental Science and Technology*, *48*(13), 7453–7460. https://doi.org/10.1021/es5013438

Otten, W., Pajor, R., Schmidt, S., Baveye, P. C., Hague, R., & Falconer, R. E. (2012). Combining X-ray CT and 3D printing technology to produce microcosms with replicable, complex pore geometries. *Soil Biology and Biochemistry*, *51*, 53–55. https://doi.org/10.1016/J.SOILBIO.2012.04.008

Peng, C., Crawshaw, J. P., Maitland, G. C., & Trusler, J. P. M. (2015). Kinetics of calcite dissolution in CO2-saturated water at temperatures between (323 and 373)K and pressures up to 13.8MPa. *Chemical Geology*, *403*, 74–85. https://doi.org/10.1016/j.chemgeo.2015.03.012

Pereira Nunes, J. P., Bijeljic, B., & Blunt, M. J. (2016). Pore-space structure and average dissolution rates: A simulation study. *Water Resources Research*, *52*(9), 7198–7212. https://doi.org/10.1002/2016WR019313

Peters, C. A. (2009). Accessibilities of reactive minerals in consolidated sedimentary rock: An imaging study of three sandstones. *Chemical Geology*, *265*(1–2), 198–208. https://doi.org/10.1016/j.chemgeo.2008.11.014

Plummer, L. N., & WIGLEY, T. M. L. (1976). The dissolution of calcite in CO2-saturated solutions at 25°C and 1 atmosphere total pressure. *Geochlmlca et Cosmochlmlca Acta*, *40*, 191–202.

Qin, F., & Beckingham, L. E. (2019). Impact of image resolution on quantification of mineral abundances and accessible surface areas. *Chemical Geology*, *523*, 31–41.

https://doi.org/10.1016/j.chemgeo.2019.06.004

Rathnaweera, T. D., Ranjith, P. G., & Perera, M. S. A. (2016). Experimental investigation of geochemical and mineralogical effects of CO2 sequestration on flow characteristics of reservoir rock in deep saline aquifers. *Scientific Reports*, *6*(1), 19362. https://doi.org/10.1038/srep19362

Ross, G. D., Todd, A. C., Tweedie, J. A., & Will, A. G. S. (1982). The Dissolution Effects of CO2-Brine Systems on the Permeability of U.K. and North Sea Calcareous Sandstones. In *SPE Enhanced Oil Recovery Symposium*. Society of Petroleum Engineers. https://doi.org/10.2118/10685-MS

Rusling, J. F. (2018). Developing Microfluidic Sensing Devices Using 3D Printing. https://doi.org/10.1021/acssensors.8b00079

Sandhu, D., Singh, A., Duranceau, S. J., Nam, B. H., Mayo, T., & Wang, D. (2018). Fate and transport of radioactive gypsum stack water entering the Floridan aquifer due to a sinkhole collapse. *Scientific Reports*, *8*(1), 11439. https://doi.org/10.1038/s41598-018-29541-0

Shiraki, R., & Dunn, T. L. (2000). Experimental study on water–rock interactions during CO2 flooding in the Tensleep Formation, Wyoming, USA. *Applied Geochemistry*, *15*(3), 265–279. https://doi.org/10.1016/S0883-2927(99)00048-7

De Silva, G. P. D., Ranjith, P. G., & Perera, M. S. A. (2015). Geochemical aspects of CO<inf>2</inf> sequestration in deep saline aquifers: A review. *Fuel*, *155*, 128–143. https://doi.org/10.1016/j.fuel.2015.03.045

Soulaine, C., Roman, S., Kovscek, A., & Tchelepi, H. A. (2018). Pore-scale modelling of multiphase reactive flow: application to mineral dissolution with production of. *Journal of Fluid Mechanics*, *855*, 616–645. https://doi.org/10.1017/jfm.2018.655

Vishal, V., Ranjith, P. G., & Singh, T. N. (2015). An experimental investigation on behaviour of coal under fluid saturation, using acoustic emission. *Journal of Natural Gas Science and Engineering*, *22*, 428–436. https://doi.org/10.1016/J.JNGSE.2014.12.020

Waldmann, S., Busch, A., van Ojik, K., & Gaupp, R. (2014). Importance of mineral surface areas in Rotliegend sandstones for modeling CO2–water–rock interactions. *Chemical Geology*, *378–379*, 89–109. https://doi.org/10.1016/J.CHEMGEO.2014.03.014

Watson, F., Maes, J., Geiger, S., Mackay, E., Singleton, M., Mcgravie, T., et al. (2018). Comparison of Flow and Transport Experiments on 3D Printed Micromodels with Direct Numerical Simulations. *Transport in Porous Media*. https://doi.org/10.1007/s11242-018-1136-9

Wen, H., & Li, L. (2018). An upscaled rate law for mineral dissolution in heterogeneous media: The role of time and length scales. *Geochimica et Cosmochimica Acta*, *235*, 1–20. https://doi.org/10.1016/J.GCA.2018.04.024

Xiong, W., Wells, R. K., Horner, J. A., Schaef, H. T., Skemer, P. A., & Giammar, D. E. (2018). CO2Mineral Sequestration in Naturally Porous Basalt. *Environmental Science and Technology Letters*, *5*(3), 142–147. https://doi.org/10.1021/acs.estlett.8b00047

Yoon, H., Chojnicki, K. N., & Martinez, M. J. (2019). Pore-Scale Analysis of Calcium Carbonate Precipitation and Dissolution Kinetics in a Microfluidic Device.

https://doi.org/10.1021/acs.est.9b01634

Yu, Z., Liu, L., Yang, S., Li, S., & Yang, Y. (2012). An experimental study of CO2–brine–rock interaction at in situ pressure–temperature reservoir conditions. *Chemical Geology*, *326–327*, 88–101. https://doi.org/10.1016/J.CHEMGEO.2012.07.030

Zhang, X., Salemans, J., Peach, C. J., & Spiers, C. J. (2002, January 1). Compaction experiments on wet calcite powder at room temperature: evidence for operation of intergranular pressure solution. (S. de Meer, M. R. Drury, J. H. P. de Bresser, & G. M. Pennock, Eds.), *Deformation Mechanisms, Rheology and Tectonics: Current Status and Future Perspectives*. Geological Society of London. https://doi.org/10.1144/GSL.SP.2001.200.01.02

Zhu, D., Hou, J., Wang, J., Wu, X., Wang, P., & Bai, B. (2018). Acid-alternating-base (AAB) technology for blockage removal and enhanced oil recovery in sandstone reservoirs. *Fuel*, *215*, 619–630. https://doi.org/10.1016/J.FUEL.2017.11.090

Zou, Y., Li, S., Ma, X., Zhang, S., Li, N., & Chen, M. (2018). Effects of CO2–brine–rock interaction on porosity/permeability and mechanical properties during supercritical-CO2 fracturing in shale reservoirs. *Journal of Natural Gas Science and Engineering*, *49*, 157–168. https://doi.org/10.1016/J.JNGSE.2017.11.004